Long Time-Scale Atomistic Modeling and Simulation of Deformation and Flow in Solids

Yue Fan and Penghui Cao

Contents

Abstract

Atom-based modeling and simulation are essential for the understanding and development of structural materials such as crystalline and amorphous metals. Classical molecular dynamics simulation enables the following of atomic-level structural evolution to elucidate the atomic processes underlying many macroscopic behaviors; however its predictive power is constrained by an intrinsic time-scale limitation. Here, we describe an alternative approach based on potential energy landscape modeling and transition state theory to probe the microscopic mechanisms controlling deformation and plastic flow observed in experiments. We survey several examples of slow deformation in crystals and

Y. Fan
Department of Mechanical Engineering, University of Michigan, Ann Arbor, MI, USA
e-mail: fanyue@umich.edu

P. Cao (✉)
Department of Nuclear Science and Engineering, Massachusetts Institute of Technology, Cambridge, MA, USA
e-mail: pcao@mit.edu

W. Andreoni, S. Yip (eds.), *Handbook of Materials Modeling*,
https://doi.org/10.1007/978-3-319-50257-1_150-1

metallic glasses to illustrate the computational algorithms used to perform the simulations and to reveal the underpinning elementary plastic processes that operate in crystalline and amorphous materials. We first show the evolution of dislocations and their interactions with obstacles over a wide range of strain rates and temperatures and discuss how they lead to macroscopic behaviors such as flow stress upturn and dislocation channeling. Then we turn to amorphous plasticity where discrete stress relaxation (avalanche) processes arise in serrated flow and creep in metallic glasses. A nonlinear interplay between nonaffine atomic displacement and local shear transformation distortion is revealed that provides a molecular explanation of the deformation-rate upturn.

1 Introduction

To meet the demand of advanced materials with unique functionalities, it is becoming increasingly important to study material performance in complex environments at the fundamental level. Computational modeling and simulation, as widely applied techniques nowadays, can provide unprecedented details on materials from atomic level. While simulations have particular advantages over "real" experiments in terms of lower cost, faster progress, and better control of isolated parameters in affecting the modeled system, there are still unsolved problems in terms of the limited spatial and temporal scales in traditional atomistic modeling techniques. The length scale issue is less challenging because even a few thousand atoms, with the use of periodic boundary condition, can reasonably represent many materials' bulk properties. In addition, the length scale limitation can, at least partially, be addressed by parallelizing the problem and exploiting supercomputer systems. However, the time step in the integration over time cannot be parallelized in the computations. This makes it a formidable challenge to reach long timescales with atomistic simulations. For example, as will be discussed below, the widely used molecular dynamics (MD) simulation can hardly go beyond nanoseconds, which is often more than ten orders of magnitude away from the timescales of the phenomena of interest in real experiments. It is therefore highly desirable to develop and employ new modeling algorithms that can address such timescale issues, while still retaining the atomistic details.

The properties of condensed matter systems are primarily governed by the interactions between constituent atoms in the system. The system's potential energy is a function of its atomic configurations. For a many-body interacting system with defects (i.e., topological disorders), there are many local energy minima, known as inherent structures, representing metastable states of the system. The hyperdimensional energy surface in configuration space is called potential energy landscape (PEL), and material microstructural evolutions correspond to the progressive exploration of different local minima in PEL (Suo 2000; Wei and Zhigang 1996). In the scope of this chapter, the microstructural evolution consists of nonequilibrium processes, which are governed by collective, rare events in the PEL. Since the activation barriers for the rare events are very high, according to transition

state theory (TST), the system will be trapped in deep energy basins for an amount of time (proportional to $\exp[\Delta E/k_B T]$, where ΔE is the activation barrier), which can be well beyond that accessible by MD. To enable long timescale modeling, an alternative approach is to proactively explore the structures of energy landscape, identify the transition pathways and barriers, and incorporate that information into TST calculations. Different atomistic algorithms have been developed, including the activation-relaxation technique (ART) (Barkema and Mousseau 1996; Cances et al. 2009), the dimer method (Henkelman et al. 1999; Haixuan et al. 2012), hyper- (or meta-)dynamics (Haixuan 1997; Laio and Parrinello 2002), temperature-accelerated dynamics (TAD) (Sorensen and Voter 2000; Bai et al. 2010), and the autonomous basin climbing (ABC) method (Kushima et al. 2009a; Fan et al. 2014; Cao et al. 2012; Yip 2016). Each technique has its own advantages and drawbacks (Fan et al. 2014; Fan 2013). In this chapter we focus on the ABC method. To the best of our knowledge, such algorithm has been found useful in both dislocation system (Fan et al. 2012, 2013; Bai and Fan 2018; Wang et al. 2013; Tao et al. 2018a,b) and amorphous system (Kushima et al. 2009a; Cao et al. 2012, 2013, 2017, 2018; Kushima et al. 2009b) as discussed below in Sects. 2 and 3, respectively. The development of original ABC algorithm (Kushima et al. 2009a) was inspired by Laio and Parrinello's idea of escaping from free-energy minima (Laio and Parrinello 2002). To be more specific, a series of penalty function are applied, and total relaxations are performed to allow the system to climb out of the local basin in the PEL. More recently the ABC method has been extended to capture the multiple competitive pathways in the PEL (Fan et al. 2014). In addition, to enhance the computation efficiency, a novel strategy termed self-learning metabasin escape (SLME) was formulated to merge the newly applied penalty function with those already added ones. Given the limited space here, we refer the readers to the original references for implementation details (Cao et al. 2012; Yan et al. 2016).

2 Evolution of Dislocations in Crystalline Materials

The mechanical behavior of structural metals is controlled by evolutions and interactions between microstructural features known as defects in the materials. Among various types of defects affecting the mechanical properties of structural materials, dislocations are one of the most critical microstructures because they are the main carriers of plastic deformation (Hull and Bacon 2011). In particular, when there are obstacles in slip planes, they will resist the glide motion of dislocations and hence significantly change the system's mechanical performance, including the yield strength, work hardening, strain-rate sensitivity, strain localization, elastic-viscoplastic behavior, etc. (Bakó et al. 2006; Bulatov et al. 2006; Brechet and Estrin 1995; Dunlop et al. 2007; Lebyodkin et al. 1995). Therefore, probing dislocation evolutions and their interactions with obstacles at various environments are the keys to understand, predict, and control mechanical properties of materials. This is a subject that has been extensively studied over the past few decades (Fan et al. 2013; Bacon et al. 2006; Domain and Monnet 2005; Dutta et al. 2012; Gordon et al. 2010;

Gussev et al. 2015; Iyer et al. 2015; Kabir et al. 2010; Kioussis and Ghoniem 2010; Norfleet et al. 2008; Onimus et al. 2004; Osetsky et al. 2006a).

Computational modeling and simulation, accompanied by the continuous enhancement of computing power, have become an effective quantitative approach in materials research, constructively complementing theories and experiments (Yip 2003). Although first principle calculations and MD studies have yielded notable advances in the knowledge of dislocation-mediated mechanics from fundamental levels, they face formidable challenges in probing the non-equilibrium phenomena at realistic timescales. To be more specific, typical MD studies on dislocations are performed either at very high strain rates greater than $10^6\ s^{-1}$ (Bacon et al. 2006, 2009; Terentyev et al. 2010a, 2008), while on the other hand, typical mechanical test experiments are performed under low strain-rate conditions, i.e., slower than $10^0\ s^{-1}$ (Dunlop et al. 2007; Onimus et al. 2004; Onimus and Béchade 2009). It has been found that intrinsic timescale limitations in conventional modeling not only could induce huge errors in yield strength quantifications (Zhu et al. 2008) but, more importantly, might provide misleading microstructural evolution mechanisms (Fan et al. 2013). Such challenge therefore calls for the development of a reliable predictive model that can capture the fundamental mechanisms at realistic timescale.

In this section we consider two examples concerning the activities of dislocations over a broad range of timescales by using the ABC-based modeling technique introduced above: (i) nonlinear variation of dislocation mobilities and onset of flow stress upturn and (ii) interaction mechanism map between dislocation and obstacle under various thermomechanical conditions.

2.1 Flow Stress of an Individual Dislocation

At low temperature, the deformation of metals is largely governed by the thermal activation of dislocation glide (Hoge and Mukherjee 1977). Experiments on different structures of metals, including Fe, Ta, Cu, Al, and Zn (Hoge and Mukherjee 1977; Ferguson et al. 1967; Kumar et al. 1968; Campbell and Ferguson 1970; Follansbee et al. 1984; Regazzoni et al. 1987), indicate the dislocation flow stress varies with strain rate in an apparently universal manner. The flow stress increases slowly in an Arrhenius manner at low strain rates but turns upward sharply beyond a certain range of strain rate. Although the results for different metals can be quantitatively different, the flow stress "upturn" behavior when the strain rate reaches the range of 10^3–$10^4\ s^{-1}$ (Regazzoni et al. 1987; Armstrong et al. 2009) appears to have a more fundamental origin. The onset of non-Arrhenius response has elicited the development of several empirical constitutive models (Hoge and Mukherjee 1977; Armstrong et al. 2009; Zerilli and Armstrong 1987; Follansbee and Kocks 1988; Steinberg et al. 1989; Preston et al. 2003; Remington et al. 2006), including the assumption of phonon drag effects to account for the data at high strain rates. All existing models to date use adjustable parameters to connect the flow stress below and above the critical strain rate for "upturn." Therefore, it would be of

interest to seek a more fundamental understanding with less postulated mechanisms or adjustable parameters.

From the PEL perspective, a dislocation line is located on the bottom of the so-called Peierls energy valley until a thermal fluctuation enables it to climb over the activation barrier to glide to the next valley. When an external stress is applied, the depth of the valley, i.e., the glide activation barrier $E(\sigma)$, can be decreased, making the dislocation easier to escape from the valley. As a result, the escape rate can be calculated by using transition state theory (TST):

$$k(\sigma) = k_0 e^{-\frac{E(\sigma)}{k_B T}} \tag{1}$$

where k_0 is the attempt frequency. The activation barrier $E(\sigma)$can be either empirically assigned or directly identified by employing ABC method at various stress levels.

In the elastic deformation regime, the dependence of stress on applied strain rate as a function of time, t, is given by

$$\sigma = G\varepsilon = G\dot{\varepsilon}t \tag{2}$$

where G is the shear modulus. The ε in Eq. (2) represents the elastic strain, because in this case study we focus on the initiation of dislocation flow, which pertains to the transition from elastic deformation regime to plastic deformation regime. In light of Eq. (2), $k(\sigma)$ can be represented as a function of time, $k(t)$.

The residence probability P(t) that the dislocation does not escape to a neighboring potential energy valley during time t (i.e., the system remains in the elastic deformation regime) is defined as Zhu et al. (2008)

$$\frac{dP(t)}{dt} = -k(t)P(t) \tag{3}$$

or

$$P(t) = \frac{1}{C}\exp\left[-\int_0^t k(t')dt'\right] \tag{4}$$

where C is the normalization factor. Accordingly, the first escape probability distribution p(t) is given by

$$p(t) = -\frac{dP(t)}{dt} = \frac{1}{C}k(t)\exp\left[-\int_0^t k(t')dt'\right] \tag{5}$$

with normalization,

$$\int_0^{t_c} p(t)dt = 1 \Rightarrow C = \int_0^{t_c} k(t)\exp\left[-\int_0^t k(t')dt'\right]dt \tag{6}$$

where $t_c = \sigma_c / G\dot{\varepsilon}$ represents the maximum residence time, at a given non-zero strain rate $\dot{\varepsilon}$. The average residence time is therefore given by

$$\bar{t} = \int_0^{t_c} tp(t)dt = \frac{\int_0^{t_c} tk(t) \exp\left[-\int_0^t k(t')dt'\right] dt}{\int_0^{t_c} k(t) \exp\left[-\int_0^t k(t')dt'\right] dt} \tag{7}$$

In the limit of vanishing $\dot{\varepsilon}$, $k(t)$is a constant, k, and $t_c \to \infty$, Eq. (7) gives the average time as $\bar{t} = 1/k$, which follows the Arrhenius law. However, for the general condition of non-zero strain rate, the result of Eq. (7) will deviate from the Arrhenius behavior.

We would like to stress here that the derivations of Eqs. (1), (2), (3), (4), (5), (6), and (7) represent a general formalism that is applicable to a wide range of systems where the reaction rate is time-dependent. Relevant examples in the present context would include dislocation nucleation under constant strain-rate loading, glass transition at different cooling rates, as well as dislocation flow. In this case study, we are particularly interested in predicting the variation of flow stress with temperature and strain rate. Since the dislocation will start to glide beyond the residence time $\bar{t}$, we obtain the flow stress by combining Eqs. (2) and (7):

$$\bar{\sigma}_{flow} = G\dot{\varepsilon}\bar{t} = \frac{\int_0^{\sigma_c} \sigma k(\sigma) \exp\left[-\frac{1}{G\dot{\varepsilon}} \int_0^{\sigma} k(\sigma')d\sigma'\right] d\sigma}{\int_0^{\sigma_c} k(\sigma) \exp\left[-\frac{1}{G\dot{\varepsilon}} \int_0^{\sigma} k(\sigma')d\sigma'\right] d\sigma} \tag{8}$$

In summary, once the dislocation migration barrier profile $E(\sigma)$ is known, the flow stress of the corresponding slip system at arbitrary thermomechanical conditions can be calculated according to Eq. (8). There is then only one parameter in Eq. (8), the attempt frequency k_0, which can be taken to be of the order of $10^{12\sim13}$ s^{-1}. Below we will apply the constitutive equations just derived to a specific example of the flow stress in bcc Fe.

The deformation of bcc metals at low temperature is known to be controlled by the motion of <111> screw dislocations (Domain and Monnet 2005), the flow mechanism being 3D kink nucleation and propagation (Gordon et al. 2010; Rodney and Proville 2009). For the purpose of testing Eq. (8), we examine a short dislocation of length 5b, b being the Burger's vector, which should glide without kink nucleation. Figure 1b above shows the glide barrier for such a dislocation in bcc Fe with an embedded-atom method-type potential developed by Mendelev et al. (2003). Clearly the barrier shows a monotonically decreasing behavior well described by a (p, q) expression $E(\sigma) = E_0\left[1 - (\sigma/\sigma_c)^p\right]^q$ (Rodney and Proville 2009; Kocks et al. 1975), where $p = 0.63$ and $q = 1.41$. For the convenience of benchmark discussion below, we also include a dashed line in Fig. 1b denoting $p = q = 1$, which is the assumption of a linear behavior with a constant activation volume.

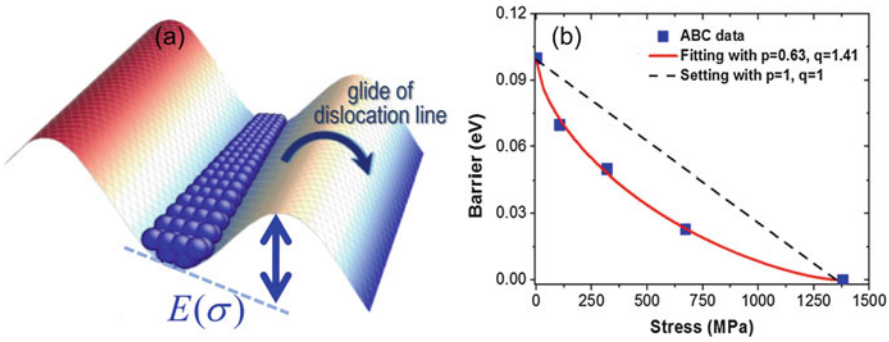

Fig. 1 (**a**) The glide of dislocation corresponds to the hopping between Peierls energy valleys. (**b**) Activation barrier for dislocation glide usually decreases as a function of applied shear stress. Blue squares are the calculated data points by ABC method, and corresponding solid curve is a fit to the realistic (p,q) expression. Dashed line represents a hypothetical linearly decreasing profile

Figure 2a shows the thermal behavior of flow stress for strain rates varying over ten orders of magnitude, from $10^7\,s^{-1}$ down to $10^{-3}\,s^{-1}$. In the low temperature limit, absence of thermal activation, all flow stresses approach the Peierls stress, which is 1400 MPa for the given potential. As temperature increases, all the flow stresses monotonically decrease. At a fixed temperature, higher strain-rate loading results in higher flow stress response, suggesting that any quantitative comparison between experimental data and MD simulations must take into account the difference in the strain rate.

The symbols in Fig. 2a represent the corresponding MD results at strain rate of $10^6\,s^{-1}$ and $10^7\,s^{-1}$. They are in reasonable agreement with the predictions of Eq. (8) using $k_0 = 1.2*10^{12}\,s^{-1}$, which matches the Debye frequency satisfactorily. This constitutes a self-consistent test of Eq. (8) with $E(\sigma)$ taken from Fig. 1b (the solid curve) in the range of strain rates where MD is valid. One can see an increasingly sharp drop of flow stress as the strain rate decreases to the range accessible to conventional experiments. The sharp drop has been known as a significant feature of the thermal activation process; this behavior is not well captured by MD simulations at its characteristic strain rates (Domain and Monnet 2005; Zhu et al. 2008). Figure 2a shows that this behavior is at least qualitatively accounted for by the present model.

The variation of flow stress with strain rate is of fundamental interest in experimental studies of crystal plasticity. Figure 2b shows the predicted behavior based on Eq. (8). Under the limit of infinitely high strain rate, the flow stress approaches the Peierls stress. On the other hand, the flow stress is negatively sensitive to the temperature. In the high temperature limit, the flow stress approaches zero regardless of the strain rate. At low $\dot{\varepsilon}$ the flow stress increases only moderately, but as $\dot{\varepsilon}$ increases, above $100\,s^{-1}$ at 50 K, and $10^4\,s^{-1}$ at 100 K, it begins to increase much more strongly. This upturn behavior can be analyzed in terms of two factors, stress-dependent activation volume and strain rate-induced non-Arrhenius behavior.

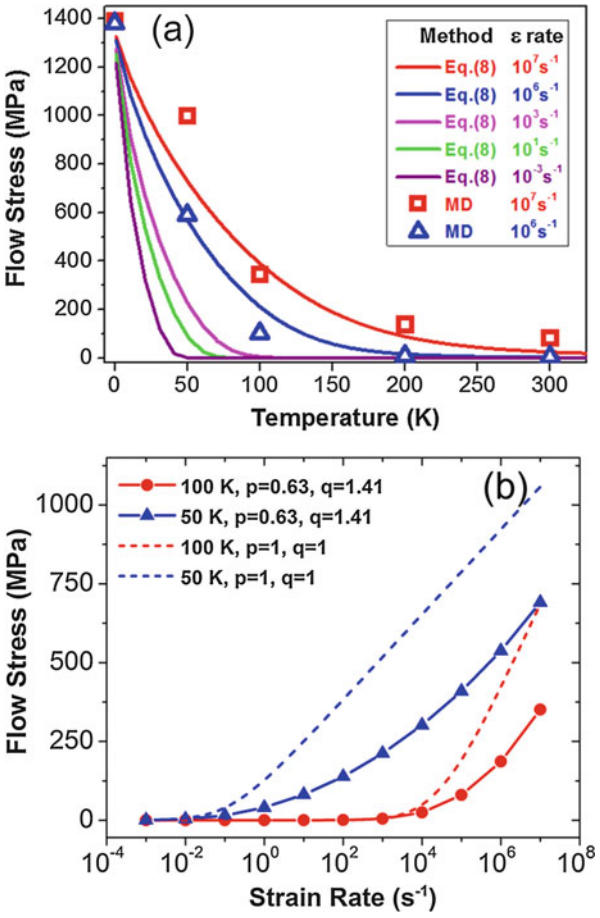

Fig. 2 (**a**) Flow stress of the <111> screw dislocation in bcc Fe under different strain-rate and temperature conditions. The solid lines show the calculated results by Eq. (8), and the data points are MD results at high strain rates. (**b**) Predicted flow stress variation at different strain rates. Solid and dashed curves are calculated based on realistic (p,q) barrier profile and hypothetical linear profile shown in Fig. 1b, respectively

Because of the nonlinear stress dependence of the activation barrier (Fig. 1b), the activation volume is very small at high stresses. Such small activation volume leads to a high sensitivity of the flow stress dependence on strain rate (Zhu et al. 2008). In addition, as derived in Eq. (7), there is a non-Arrhenius behavior due to the strain-rate loading which also contributes to the upturn in Fig. 2b. To decouple the two contributions, we remove the nonlinearity of $E(\sigma)$ by setting p and q equal to unity (dashed line in Fig. 1b). Now the only nonlinear factor comes from the strain rate-induced non-Arrhenius behavior in Eq. (8). As shown in Fig. 2b, under this condition, the flow stress upturn remains, but the stress is now higher beyond the crossover strain rate. Since the assumption of $p = q = 1$ results in a higher effective barrier and correspondingly a longer residence time, it follows that the flow stress response is higher as well. Our analysis therefore shows the onset of flow stress upturn is to be attributed mainly to the non-Arrhenius behavior induced by strain rate, as described by Eqs. (7) and (8).

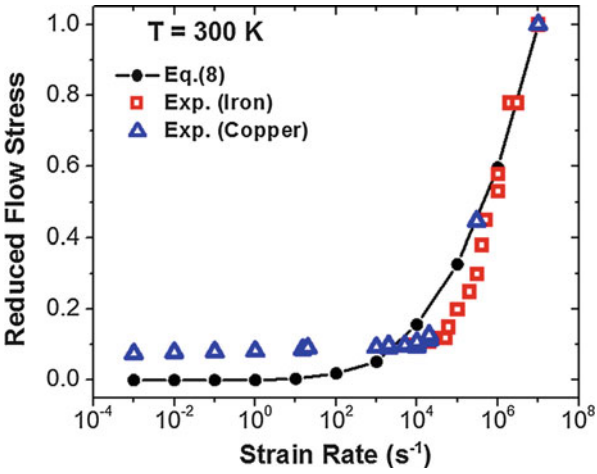

Fig. 3 Variation of reduced flow stress with strain rate at 300 K. (The experimental data on copper and ion are adapted from Armstrong et al. (2009) and references therein)

To compare the predicted upturn behavior quantitatively with experimental data, we adapt the energy profile $E(\sigma)$ for a longer screw dislocation system in bcc Fe calculated by Gordon et al. (2010) and use it as the input into Eq. (8). Figure 3 shows the variation of flow stress and strain rate at 300 K, as observed experimentally and predicted by our model. Since the flow stress magnitude is significantly influenced by the defect microstructures in the experimental specimens (Armstrong et al. 2009), the quantitative comparison can only be meaningful after an appropriate normalization. Therefore, in Fig. 3, we show the reduced flow stress, defined as the ratio of flow stress to its value at the highest strain rate $10^7\ \mathrm{s}^{-1}$, as a function of strain rate. It is seen that both the experiments and our calculation results show a significant flow stress upturn with the critical strain rate in the range of 10^4–$10^5\ \mathrm{s}^{-1}$. The extent of the agreement suggests Eq. (8) and $E(\sigma)$ have essentially captured the mechanism for the flow stress upturn behavior. On the other hand, it is known that the flow stress magnitude depends on the local defect microstructure in the material. Experimental specimens have a complex defect microstructure leading to appreciably higher flow stresses (due to, e.g., dislocation-obstacle interactions to be discussed in the next section) seen in the experiments compared to the results in Fig. 2b. It is therefore intriguing that the reduced flow stress predicted by our model in Fig. 3 is also quantitatively consistent with experiments from different materials (a ductile one, copper, and, a brittle one, iron). This may be attributed to the fact that the energy barrier for dislocation to climb/glide over the defects/obstacles in the material bears a similar stress-activated behavior as the simple dislocation glide represented by the expression $E(\sigma) = E_0\left[1 - (\sigma/\sigma_c)^p\right]^q$ that was described above (Remington et al. 2006).

In sum, such example shows that, without invoking any specific mechanism or fitting parameters, the PEL-based approach can naturally capture the nonlinear transition of the flow stress from a classical Arrhenius behavior to a fast upturn over a broad range of strain rates.

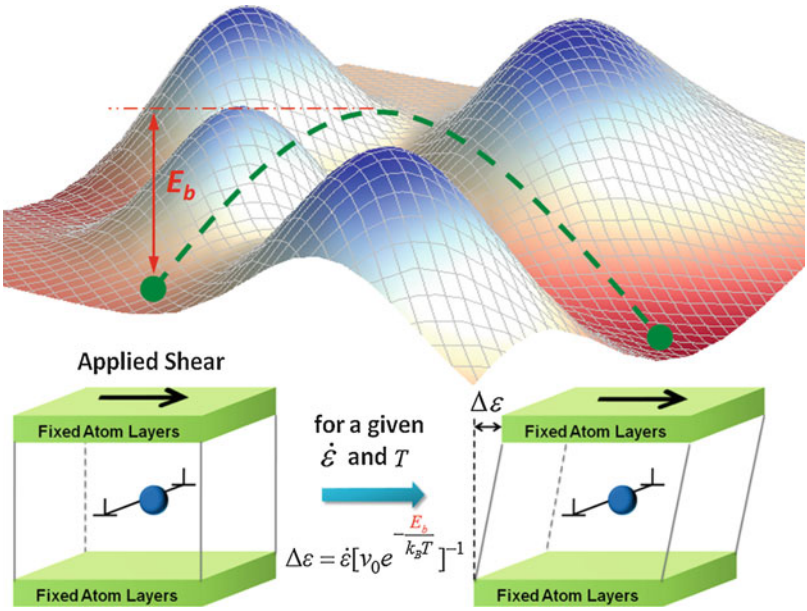

Fig. 4 Schematic ABC-TST modeling on dislocation-obstacle interaction at prescribed thermo-mechanical conditions. The detailed iterative procedures are described in the main text

2.2 Dislocation-Obstacle Interaction Mechanism Map

Under complex environments (e.g., irradiation, severe plastic deformation, etc.), a host of non-equilibrium obstacles/precipitates would be present in the system. It therefore becomes particularly important to probe the dislocation-obstacle interaction mechanisms at various conditions since they will determine many important mechanical properties of structural materials, such as hardening, creep, embrittlement, crack nucleation, etc. (Bakó et al. 2006; Bulatov et al. 2006; Jumonji et al. 1996; Van der Giessen et al. 2001; Shin et al. 2005).

The first key challenge that needs to be addressed is to investigate the dislocation-obstacle interactions at much longer timescale, well beyond the range accessible to MD. As introduced above, the ABC method is a robust algorithm that can drive the system out from a trapped deep energy basin and thus probe the microstructural evolution at long timescales. Therefore, by iteratively combining ABC and TST into a dynamic scenario, one could then study the dislocation-obstacle interactions at prescribed strain rate and temperature, as illustrated in Fig. 4.

The consecutive iterations can be described as:

1. Under a given strain condition (including the initial state with no strain), employ ABC to explore the PEL structure, and thus obtain the dominant reaction pathway at this moment.

2. Apply nudged elastic band (NEB) method to accurately calculate the energy barrier E_b between the current and next minimum states in PEL that are identified in step (i).
3. Determine the thermal activation time defined as $\Delta t = [\nu_0 \cdot \exp(-E_b/k_B T)]^{-1}$, where $\nu_0$is the attempt frequency (of Debye order 10^{13} s^{-1}). For a specified strain rate$\dot{\varepsilon}$, the corresponding strain increment, $\Delta\varepsilon = \dot{\varepsilon} \cdot \Delta t = \dot{\varepsilon}\ [\nu_0 \cdot \exp(-E_b/k_B T)]^{-1}$, is applied to the system. Go back to step (i) under the new strain condition.

Through this algorithm, the coupling between thermal activation and strain rate is treated in the transition state theory framework. To be more specific, because ABC is employed iteratively on-the-fly, the environmental effects on PEL will be naturally captured. Since the atomic arrangements near the defects (e.g., dislocations and obstacles) are off perfect lattice sites and highly disordered, the underlying PEL structures could be rather complex, and each local minimum state in PEL might connect with multiple different transition pathways, corresponding to different evolution mechanisms. If these transition pathways show different sensitivities to surrounding environments (e.g., strain rate, temperature, stress state, etc.), then a crossover between their relative importance at different conditions might occur, which would then lead to different deformation mechanisms and mechanical behavior.

Figure 5 shows an example on the interaction mechanisms between a $< 11\bar{2}0 >$ $\{10\bar{1}0\}$dislocation and a self-interstitial atom (SIA) cluster in HCP Zr over a wide range of thermomechanical environments (Fan et al. 2013). Starting from the initial state in Fig. 5a, the PEL-based iterative ABC-TST procedure enables one to uncover the interaction mechanisms over 15 orders of magnitude in timescales, from 10^7 s^{-1} down to 10^{-7} s^{-1}, far beyond the MD's range but appropriate for direct comparison with experiments. It is demonstrated in Fig. 5b that even the same unit process could lead to remarkably different mechanisms. Specifically, in the low temperature and high strain-rate regime, the dislocation tends to simply pass by the obstacle, and the system undergoes a stable homogeneous deformation with normal work hardening, while in the higher temperature and lower strain-rate regime, the obstacle is absorbed and swept by the dislocation. The removal of obstacle will result in a defect-free region along the slip plane known as dislocation channel, which is associated with strain localization and heterogeneous deformation, and could further induce mechanical instability.

The reason why the same initial state could give rise to significantly different mechanical behavior can be explained by the environmental effects on the system's underlying PEL structure revealed by the ABC technique. As shown in Fig. 5c, for such unit process in HCP Zr, the initial state connects with two transition pathways that are associated with different microstructural evolution modes. At the beginning, path I (obstacle removal) has a lower activation energy than path II (simple bypass) does. Therefore, if the surrounding environments do not change significantly, say when the driven strain rate is relatively low, then the system would naturally

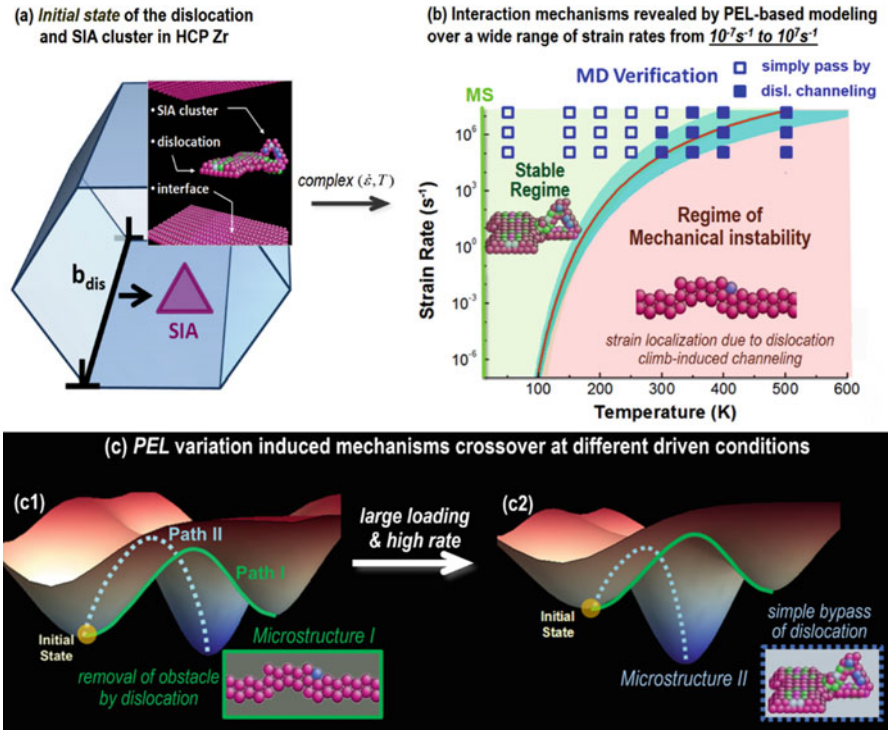

Fig. 5 (**a**) Initial state of the unit process of dislocation-SIA cluster interaction in the prismatic slip system in HCP Zr. (**b**) The same initial state could result in remarkably different evolution mechanisms when the timescale is spanning more than 15 orders of magnitude. In the low temperature and high strain-rate regime, the system undergoes a stable homogeneous deformation process because the dislocation simply bypasses the SIA cluster. However, in the higher temperature and lower strain-rate regime, the SIA cluster is absorbed and removed by the gliding dislocation, which then leads to dislocation channeling and mechanical instabilities. It can be seen that the ABC-based modeling technique allows one to probe the microstructural evolution mechanisms from atomic level at realistic timescale far beyond the traditional MD's range (region of blue squares). (**c**) The crossover of two different mechanisms originates from the variation of system's underlying PEL under different environments. As shown in (c1), the initial state connects with two transition pathways that are associated with different microstructural evolution modes. At the beginning, path I (obstacle removal) has a lower activation energy than path II (simple bypass) does. Therefore, if the driven strain rate is relatively low, i.e., when the surrounding environments do not change appreciably, then the system would naturally have a higher chance to go through the path I, which leads to obstacle removal. On the other hand, under very high strain-rate scenario, since path II is more sensitive to external loading and its activation barrier under large strain becomes lower than path I does, as seen in (c2), then path II becomes more favorable and a bypass mechanism occurs

have a higher chance to go through the path I and give rise to the dislocation channel formations. This is indeed what has been observed by TEM experiment (Onimus et al. 2004) at the condition of 600 K and 10^{-4} s^{-1}. However, as shown in Fig. 5c1–c2, the responses of two pathways to external stimuli are different. Path

II is more sensitive to the applied shear loading, and its activation barrier becomes lower at large strain condition. Therefore, under very high strain-rate scenario, path II becomes favorable very quickly, and a different deformation mechanism would occur.

To validate the diagram just predicted, independent MD simulations have been employed. Although MD studies are limited to the very high strain-rate regime, the results at different temperatures (blue squares in Fig. 5b) show a clear mechanism crossover between dislocation bypass and channeling.

We would like to note that the approach in constructing the mechanism map is based on a general thermal activation theory under prescribed strain rate (Fan et al. 2012, 2013), and is not limited to the defects discussed here in the Zr system. For instance, previous MD simulations in bcc Fe report different interaction mechanisms between a dislocation and a SIA loop as a function of temperature (Terentyev et al. 2010a; Bacon et al. 2009). Specifically, at high temperature, the SIA loop is absorbed by the dislocation, while at low temperature, both dislocation and SIA loop are completely recovered. Despite both being at high strain rate, these two different outcomes in bcc Fe can also be understood as a competition of strain rate and temperature, as explained by the mechanism map in Fig. 5b. In other words, the present framework is quite general and can be applied to study different materials (e.g., glass materials, colloidal system) and responses to different conditions (e.g., annealing rate, irradiation rate).

3 Plasticity in Amorphous Solids

Glassy materials deform and flow in response to external mechanical agitation and internal thermal activation. Due to the lack of well-defined structural defects such as dislocations in their crystalline counterpart, studying the mechanistic details, by which the constituent atoms rearrange themselves under stress and temperature environment, is still not well understood. In particular, the stress and strain-rate effects on plastic deformation and its underlying microscopic processes are in need of further studies.

A number of theoretical models have been proposed to describe the mechanisms of atomistic deformation and flow responsible for plastic deformation in amorphous solids. Spaepen considered the distinction between homogeneous and inhomogeneous flows in metallic glasses (Spaepen 1977) and introduced the concept of the local free volume as an order parameter. In this view local strain production and dissipation are assumed to be associated with individual atomic jumps. Argon proposed a plastic deformation model of metallic glasses based on the notion of local shear transformations driven by stress and in the presence of thermal fluctuations (Argon 1979). The atoms participating in such processes essentially undergo an inelastic shear deformation. Twenty years later, Falk and Langer introduced the term shear transformation zone (STZ) in interpreting simulation results of viscoplastic deformation of amorphous solids (Falk and Langer 1998), and the term STZ has become widely adopted in studies of amorphous materials.

On the other hand, significant attempts to understand amorphous plasticity have been carried out using molecular dynamics (MD) simulations. For instance, MD results revealed that structural disorder-induced softening precedes thermal softening which acts as the origin of the shear banding (Cao et al. 2009). The bottleneck well-known in MD is that simulations of deformation often entails extreme conditions of strain rate which are higher by several orders of magnitude than those studied experimentally (Yamakov et al. 2002; Sentjabrskaja et al. 2015). Because slow thermal activations and relaxations could be suppressed due to the short timescale in MD simulations, direct comparison with experiments cannot be straightforwardly performed.

In this section, we discuss two studies of amorphous plastic deformation under low mechanical stress or slow strain rate using the ABC-based PEL sampling technique: (1) constant stress-driven amorphous creep and (2) strain rate-dependent slip avalanches in amorphous plasticity.

3.1 Creep: Deformation and Flow at Constant Mechanical Stress

Creep is a slow deformation phenomenon occurring in materials typically subjected to constant mechanical stress and temperature. Creep deformation has been studied in various amorphous materials such as metallic glasses and colloidal systems (Krisponeit et al. 2014; Huang et al. 2009; Siebenbürger et al. 2012; Schuh et al. 2007; Lu et al. 2003). To identify the elementary processes of deformation and flow in amorphous creep, we implement a meta-dynamic formulation (Cao et al. 2017) that allows transition state trajectories to be generated on timescale of seconds. In the simulation, we apply a prescribed uniaxial tensile stress to the system and execute the following steps:

1. Perform energy minimization on the relaxed system to bring it to the nearest local energy minimum.
2. Apply the autonomous basin climbing (ABC) algorithm (Kushima et al. 2009a; Cao et al. 2012) to obtain the transition state pathway and determine the neighboring local energy minimum state.
3. Compare the internal stress of the new state with the prescribed tensile stress. If the two stresses deviate by more than 1%, perform step (d); otherwise go back to step (b).
4. Perform cell relaxation in the presence of the external stress. The atoms are rescaled to new positions whenever the size of simulation cell is changed, and the final configuration converges to a new local minimum.

The system evolution is then determined by examining the newly sampled configurations of the local energy minima. The activation time of each evolution step can be estimated through transition state theory, $\Delta t_i = \left[\upsilon_0 \exp(-\frac{\Delta E_i}{k_B T})\right]^{-1}$,

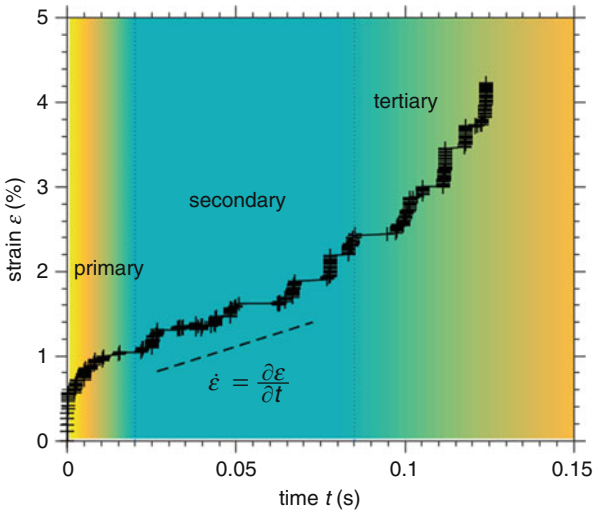

Fig. 6 Simulated creep curve: time evolution of system strain ε at stress 198 MPa and temperature $0.68T_g$. The creep rate $\dot{\varepsilon}$ of the secondary stage is essentially constant and at a minimum. The background colors are drawn schematically to denote the creep rate

with attempt frequency v_0 typically taken to be 10^{12} s^{-1}, ΔE_i is the energy barrier of activation path i.

Figure 6 shows the simulation result of time development of the system strain. The creep curve shows the classical behavior of three stages of strain evolution. The initial period of strain buildup, consisting of a steep increase followed by a gradual approach to saturation, is known as primary or transient creep. The secondary stage of steady-state creep is a period of linear strain increase in time. The extent of this stage depends on the combination of applied stress and system temperature. For relatively low stresses, the secondary stage may have a considerable extent before the onset of tertiary creep, where strain rate increases without apparent limit. In the case of Fig. 6, the onset of structural instability at a strain level of ∼2.5% is readily observed.

In the present discussion, our interest lies in the mechanisms sustaining the steady-state creep (secondary stage). By varying the value of applied stress, one can determine the creep rate, and its variation with stress is shown in Fig. 7a. We can see a bimodal behavior in the monotonic variation of creep rate $\dot{\varepsilon}$ with stress σ. At low stress, $\dot{\varepsilon}$ is characterized by a creep-rate slope of $n \sim 1.5$, where n is known as the stress exponent. At high stress n increases to ∼5. Notice the stress value for the change in index n. The transition in creep rate behavior is well-known in experiments on different materials (see Fig. 7b for comparison with experiments) (Boyle and Spence 2013; Nieh and Wadsworth 2006; Klueh 2005). It is generally understood to signify thermal activation processes at low stress, changing over to

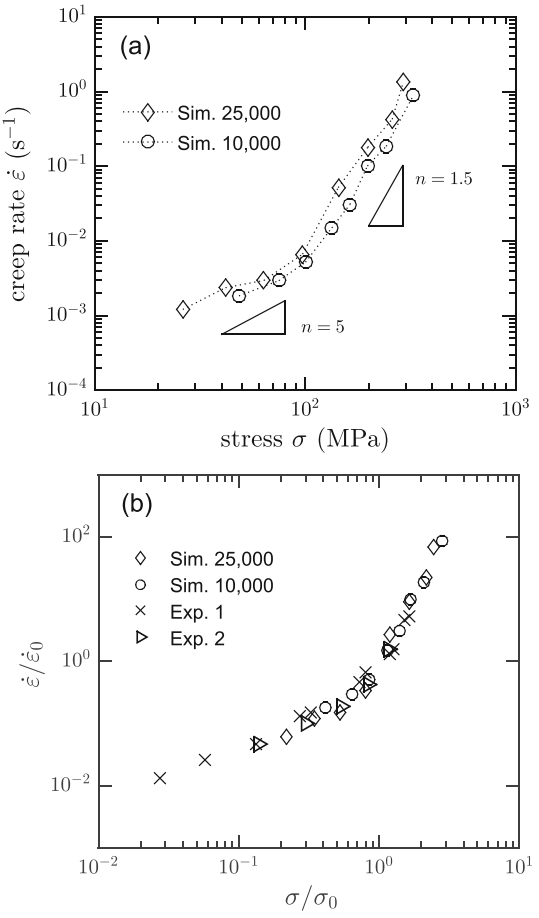

Fig. 7 (**a**) Stress dependence of creep rate from simulations with two different system sizes of 25,000 and 10,000 atoms. (**b**) Stress variation of creep rate, the two sets of experimental data 1 (crosses) and data 2 (triangles) are adapted from Lu et al. (2003) and Nieh and Wadsworth (2006), respectively. σ_0 and $\dot{\varepsilon}_0$ are threshold values in the creep rate-stress curve

stress activation for reasons that have not been resolved heretofore, particularly regarding the roles of atomic diffusion and shear deformation.

Figure 8 shows the spatial distributions of nonaffine displacement and of deviatoric strain at low and high stresses. At the low stress of 64 MPa, the features of the nonaffine displacement and local strain can be essentially attributed to thermally processes. As shown in Fig. 7c, the thermally activated atomic diffusion produces little local strain burst (local rupture) event. At high stress of 258 MPa indicated by Fig. 8b, the displacement magnitude of the sites of high mobility is about a factor of three larger than the displacements at low stress. Moreover, when looking at Fig. 7d, we see the presence of bi-directional deformation which corresponds to local strain bursts, a striking effect of stress-induced deformation.

We believe the creep rate upturn delineates a regime of nonlinear response in the rheological behavior of amorphous materials, a consequence of the nonlinear coupling between atomic diffusion and shear-induced deformation. More generally,

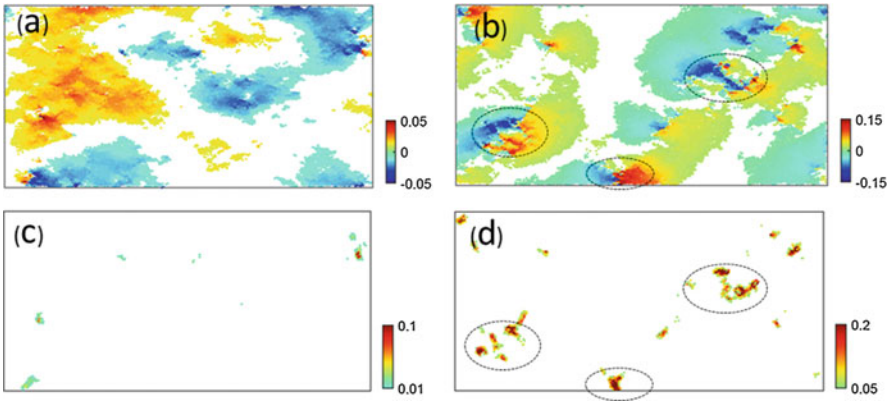

Fig. 8 Spatial distributions of nonaffine displacement (**a**) and (**b**) and of deviatoric strain (**c**) and (**d**). All measures are time incremental, taken over a time interval of 0.01 s. Atoms are colored according to magnitude of their displacements or strains. At each level the left and right panels denote low stress (64 MPa) and high stress (258 MPa), respectively

it indicates an interplay between thermal and stress-activated processes, involving loading effects, thermal noise, and stress-induced fluctuations.

3.2 Slip Avalanches of Amorphous Plasticity Under Constant Strain Rates

Discrete stress relaxations (slip avalanches), the serrations in stress-strain responses to mechanical deformation are ubiquitous in the dynamics of amorphous plasticity (Schuh et al. 2007; Antonaglia et al. 2014a). A common characteristic of slip avalanches is the strain-rate sensitivity which becomes more pronounced as the rate is lowered (Schuh et al. 2002, 2007; Antonaglia et al. 2014b; Harris et al. 2016). To understand the atomistic mechanisms of stress relaxation at a wide range of strain rate, we implement an atomistic simulation algorithm (Cao et al. 2014a, 2018) that can reach timescales in the range of experiments. To model constant strain-rate simulation, we first select a strain-rate value and use the transition state theory expression $\dot{\varepsilon} = \dot{\gamma_0} \exp(-E_b/k_B T)$ to determine a value for the activation barrier E_b, where γ_0 is the attempt frequency prefactor and k_B is the Boltzmann constant. After determination of the activation barrier E_b for a strain rate $\dot{\varepsilon}$, we perform the following steps:

1. Perform energy minimization to bring the system to the nearest local energy minimum state.
2. Run the autonomous basin climbing (ABC) algorithm (Cao et al. 2012) to generate a transition state pathway (TSP) trajectory consisting of local energy

minima and saddle points, stopping the ABC simulation when an activation energy barrier greater than E_b is found.
3. Examine the local energy minima explored by the ABC algorithm, and perform a standard Monte Carlo (MC) run to pick the most likely state according to the probability $p = \exp\left(\Delta E_{(i,j)}/k_{\mathrm{B}}T\right)$, where $\Delta E_{(i,j)}$ is the energy difference between local minima i and j. Save the associated atomic configurations.
4. Apply a small strain increment $\Delta\varepsilon = 10^{-4}$ to the system, perform energy minimization, and repeat steps 1, 2, and 3. Each step thus contributes a strain increment $\Delta\varepsilon$ to the overall imposed strain ε. The associated atomic configurations stored in the process can be used to calculate the corresponding single-atom displacement and the local deviatoric strain. The iteration continues until the strain ε reaches 18%.
5. For quasistatic (QS) simulation, $E_b = 0$, so there is no need to run steps 2 an 3. The simulation thus consists of iterating on steps 1 and 4, performing energy minimization after each strain increment.

In Fig. 9a we show the simulated responses of system-level stress to uniaxial compression at three distinct values of strain rates. The curve QS (quasistatic) (Falk and Maloney 2010) is obtained by potential energy minimization, which is effectively the limit of high strain rate (Fan et al. 2013; Cao et al. 2014b). The other two curves correspond, respectively, to constant strain rates of $2.2 \times 10^{7}\,\mathrm{s}^{-1}$ and $4.6 \times 10^{-2}\,\mathrm{s}^{-1}$, which are typical of conventional MD simulations and laboratory mechanical testing, respectively.

The overall response at each strain rate shows initially elastic loading up to a yield point, followed by a series of stress drops of varying magnitudes. The effects of strain rate are first a lowering of the entire stress-strain curve as the strain rate decreases from QS to MD to laboratory testing. Secondly, a significant sharpening of the serrations occurs in this progression of strain rates. The variation of the peak (yield) stress with strain rate, known as the stress overshoot, is also evident. In Fig. 9b portions of the flow curve at the three strain rates are shown in greater detail to illustrate the significant sharpening in avalanche response as the strain rate is lowered (Maaß et al. 2011; Antonaglia et al. 2014b). At the lowest strain rate, we see well-resolved intermittent minor relaxations interspersed between large events throughout the entire flow regime. Similar behavior, suggesting a distinction between small and large avalanches, is observed experimentally (Antonaglia et al. 2014a; Wright et al. 2013; Maaß et al. 2011).

In Fig. 9c we show the corresponding deformations at the lowest strain rate associated with the onset of yielding and subsequent flow. In the four panels, one sees the spatial distributions of atomic sites with high deviatoric strain, color coded to indicate the magnitude of D^2_{min}. The distributions are cumulative strains (with reference to the initial undeformed configuration) during compression at the four numbered stages labeled in Fig. 9a: during elastic loading (point 1), after yielding (2), and during serrated flow (3–4). At 4% strain, we see only a few high-strain sites distributed rather randomly. Immediately after the onset of yielding, at 4.83% strain, a band of high-strain sites spanning the system has clearly formed. Notice also the

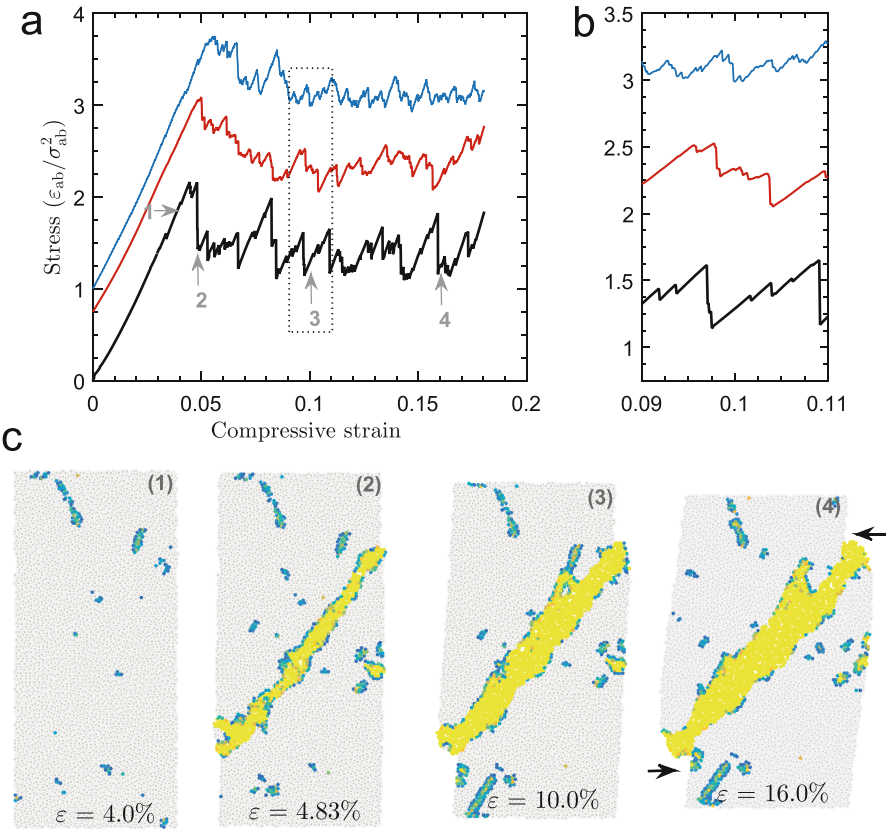

Fig. 9 (**a**) Stress-strain response obtained at three strain rates: QS (top), $2.2 \times 10^7\ s^{-1}$ (middle), and $4.6 \times 10^{-2}\ s^{-1}$ (bottom). The two upper curves have been shifted vertically by 1.0 and 0.75, respectively, to facilitate visual inspection. Arrows indicate the four stages of deformation corresponding to the four panels shown in (**c**). (**b**) Enlarged view of dotted box in (**a**). (**c**) Deviatoric strain distributions in the elastic response regime, after yielding and during the flow stage at a strain rate of $4.6 \times 10^{-2}\ s^{-1}$. The red spheres indicate atoms subjected to large deviatoric strain, and atoms with strain $D^2_{min} < 1$ are colored gray. The arrows point to surface steps at strain of 16.0%. (Images modified from Cao et al. 2018)

appearance of a surface step. After the appearance of the shear band, the subsequent plastic flow is essentially dominated by this shear localized region, involving sliding and thickening. For example, with further compression through 10% to 16% strain, the shear band has expanded in thickness as shown in the third and fourth panels of Fig. 9c. Correspondingly, the edge steps have become larger to accommodate the increased strain in the system (Shan et al. 2008).

To probe the nanoscale deformation and flow processes associated with an avalanche, we examine the deviatoric strain D^2_{min} and the nonaffine atomic displacement. Figure 10 shows the spatial maps of D^2_{min} for small and large avalanches

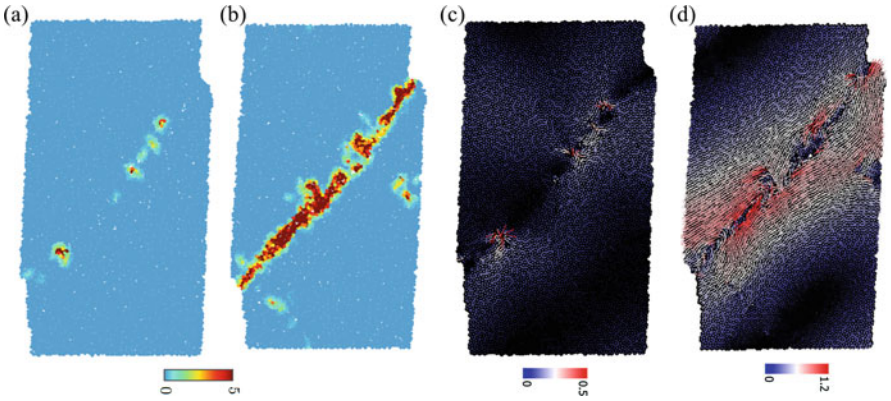

Fig. 10 Visualization of local plastic strains associated with two typical avalanches, small (**a**) and large (**b**). Atoms are color coded by the magnitude of $D^2_{\min}$. The imposed strains in the two cases are 8.3% and 9.7%, respectively. Visualization of nonaffine displacement associated with small (**a**) and large (**b**) avalanches. Arrows are color coded by the nonaffine displacement magnitude. Note that the color scale is different for (**a**) and (**b**). The imposed strains in the two cases are 8.3%

at the steady-state flow stage of deformation. In Fig. 10a, which pertains to small avalanches, one sees a few local sites of significant strain magnitude. This indicates that during a minor stress drop, there is relatively little activity involving localized shear transformations, and the few activated sites are spread out along the established shear band. In contrast, as seen in Fig. 10b, major stress relaxations involve a large number of activated sites at high strain magnitudes, clustered along a characteristic band-like region. Comparing Fig. 10a, b, one has a clear picture of the different roles that small and large avalanches play in maintaining serrated flow. Through the nonaffine displacements, we can assess atomic motions associated with internal relaxation during system flow. In Fig. 10c–d, we again see the distinction between small and large avalanches now visualized through the nonaffine atom displacement. Comparing these results with the distributions of plastic strain production, we have a consistent picture of the molecular processes associated with serrated flow, resolved between small and large avalanches and between the single-particle (diffusion) and collective (cluster deformation) degrees of freedom. The processes are clearly spatially heterogeneous and temporally intermittent. Such details provide meaningful complements to current studies of the mechanisms of amorphous plasticity, based on combining theoretical modeling (Antonaglia et al. 2014a) with high temporal resolution mechanical testing (Wright et al. 2016).

The fact that the system response is different in avalanche sizes implies the existence of two response regimes. The actual evolution of avalanche size suggests the small avalanches can be regarded as precursor events or an incubation stage leading up to the occasional major relaxation event. We see the large avalanches as a form of nonlinear response involving the concerted action of thermally activated atomic diffusion and stress-activated shear of local clusters of atoms. Such responses

are characterized by spatial and temporal fluctuations that have been referred to as dynamical heterogeneities. Recognition of this kind of response can stimulate further theoretical work in modeling the weakening mechanism that underlies the onset of avalanches.

4 Summary and Outlook

It is widely appreciated that material microstructural evolution is an immensely complicated multi-physics phenomenon involving spatial and temporal scales ranging over many orders of magnitude. To establish a modeling and simulation framework to address the fundamental molecular mechanisms and to transfer such details to the higher-level models at meso- and macroscales is certainly a grand challenge.

As an example, Fig. 11 represents a well-accepted paradigm for the multiscale modeling of dislocation-related problems. At the macroscopic scale or continuum level, the finite element method (FEM) has been regarded as the most appropriate technique (Needleman and Van der Giessen 2005; Zhong and Zhu 2008). The fidelity of FEM calculation largely depends on whether its mesh can be efficiently handled and whether there are reliable constitutive descriptions for all the nodes. The constitutive equations for dislocation-mediated deformation are usually provided by mesoscale models, such as dislocation dynamics (DD) and visco-plastic self-consistent (VPSC) method, which have been widely applied (Lebensohn et al. 2007; Turner et al. 1999; Schwarz 1999; Zbib and de la Rubia 2002; Arsenlis et al. 2007; El-Awady et al. 2008). On the other hand, both DD and VPSC models rely on many fitting or empirically assigned parameters, such as the dislocation core structures, the critical resolved shear stress for each slip system, the strain hardening exponent, the dislocation jog/junction formation mechanisms, the dislocation climb rate, etc.. As a result, although these mesoscale models can explain many observed experiments by adjusting various parameters, the predictive power of those models remains to be further improved. To reduce the number of empirical parameters, one still needs to employ more fundamental yet computationally more expensive modeling from the atomic levels, such as first principle calculations and MD method. These atomistic simulations can capture the dislocation core structures at equilibrium environments (Dezerald et al. 2016; Chaari et al. 2014; Proville et al. 2012) and provide useful mechanistic insights into the detailed dislocation-obstacle interaction processes (Terentyev et al. 2008, 2010a,b; Osetsky et al. 2006b).

Therefore, to enable a high-fidelity multiscale modeling, the connection between atomic-scale modeling and mesoscale modeling plays a vital role, because the robustness of multiscale modeling largely relies on whether MD simulations can provide accurate and complete mechanisms or not. Unfortunately, there are circumstances where MD simulations at short timescales cannot represent the realistic mechanism in experiments. An example that supports this is a remarkable controversy between the MD prediction and experimental observation over the dislocation-obstacle interaction mechanism in FCC metals. As shown in the right

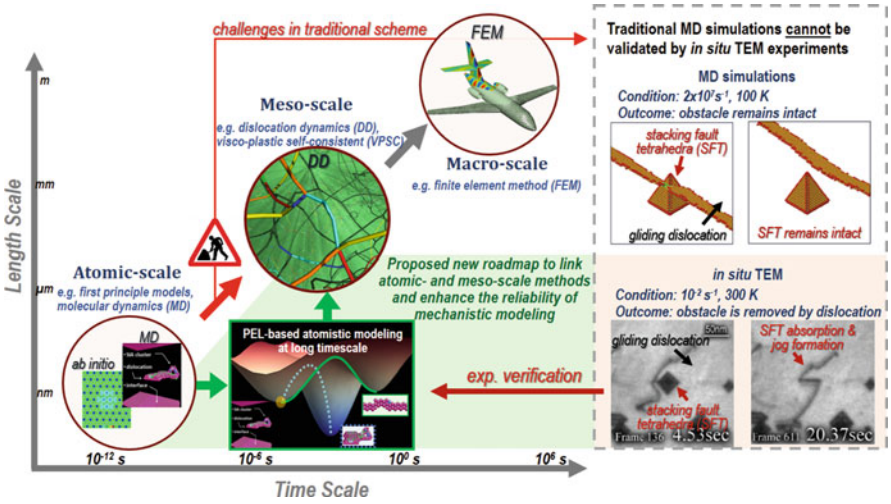

Fig. 11 Typical paradigm of multiscale modeling on dislocation-related problems consists of three different levels. At atomic scale, first principle calculation (e.g., ab initio) and molecular dynamics (MD) are widely used. At mesoscale, dislocation dynamics (DD) and visco-plastic self-consistent (VPSC) methods are most popular. And at macroscale, finite element method (FEM) is the dominant technique. It is expected that the outcomes from finer-scale models are fed into higher-level models as input parameters, which would then enable the inclusion of multi-physical processes at different scales. However, such traditional scheme, particularly the interface from MD to DD/VPSC, could be ill-informed. To be more specific, the right box shows the interaction mechanisms between a gliding dislocation and a stacking fault tetrahedra (SFT, a vacancy-type cluster) in FCC metals probed by MD simulation and by in situ TEM experiment, respectively. In MD study the SFT is found intact after cutting by the dislocation. But in real experiment, where the timescale is ten orders of magnitude longer than in MD simulation, the SFT is apparently absorbed and removed by the dislocation. Such discrepancies demonstrate that, due to its intrinsic timescale limitation, traditional MD simulation cannot capture the accurate and complete knowledge needed for the higher-level models. Given recent progress on the long-timescale atomistic simulation techniques, a new path via the PEL-based modeling has shown great promise in probing materials behavior at realistic timescale while still retaining the atomistic details

box of Fig. 11, in situ TEM experiments clearly show that a perfect SFT (a vacancy-type defect cluster named stacking fault tetrahedra) is fully absorbed and removed by a single moving dislocation (Osetsky et al. 2006a,b). However, parallel MD simulations show that the same type of obstacle remains intact after cutting by a moving dislocation (Matsukawa and Zinkle 2004). While the geometries and boundary conditions have been regarded as potential factors that might lead to such discrepancy (Osetsky et al. 2006a), the most probable reason, as discussed by Matsukawa and Zinkle (Matsukawa and Zinkle 2004), is the huge gap in timescale between the in situ TEM ($\sim 10^{-2}$ s^{-1}) and MD simulations ($\sim 10^{8}$ s^{-1}).

In this chapter we have shown several examples in both crystalline and amorphous materials that the PEL-based novel modeling techniques are capable of uncovering the microstructural evolutions over wide range of timescales and directly

compare with experimental observations (Fan et al. 2012, 2013). A particularly notable feature of the PEL framework is that it is fundamentally governed by the interatomic potentials between the constituent particles, and thus no phenomenological assumptions or empirical parameters are needed.

Given these advantages, one could propose a "detour" on the conventional multiscale modeling roadmap. As illustrated by the green arrows in Fig. 11, instead of directly connecting MD with mesoscale methods (Yip and Short 2013), one can first employ the PEL-based modeling to gain a more comprehensive knowledge at longer timescale and then pass the atomistic insights obtained on-the-fly to the higher-level models. Such a modification may be expected to lead to a more predictive modeling and simulation.

Acknowledgements The authors would like to take the opportunity to thank Sidney Yip for the instrumental discussions in outlining this chapter and for the edits. PC acknowledges the support from the US Department of Energy NEUP Grant DE-NE0008450. YF also acknowledges the support from the US Army Research Office Grant No. W911NF-18-1-0119.

References

Antonaglia J, Wright WJ, Gu X, Byer RR, Hufnagel TC, LeBlanc M, Uhl JT, Dahmen KA (2014a) Bulk metallic glasses deform via slip avalanches. Phys Rev Lett 112(15):155501

Antonaglia J, Xie X, Schwarz G, Wraith M, Qiao J, Zhang Y, Liaw PK, Uhl JT, Dahmen KA (2014b) Tuned critical avalanche scaling in bulk metallic glasses. Sci Rep 4:4382

Argon AS (1979) Plastic deformation in metallic glasses. Acta Metall 27:47–58

Armstrong RW, Arnold W, Zerilli FJ (2009) Dislocation mechanics of copper and iron in high rate deformation tests. J Appl Phys 105(2):023511–023517

Arsenlis A, Cai W, Tang M, Rhee M, Oppelstrup T, Hommes G, Pierce TG, Bulatov VV (2007) Enabling strain hardening simulations with dislocation dynamics. Model Simul Mater Sci Eng 15(6):553

Bacon DJ, Osetsky YN, Rong Z (2006) Computer simulation of reactions between an edge dislocation and glissile self-interstitial clusters in iron. Philos Mag 86(25–26):3921–3936

Bacon DJ, Osetsky YN, Rodney D (2009) Chapter 88 dislocation–obstacle interactions at the atomic level. In: Hirth JP, Kubin LP (eds) Dislocations in solids, vol 15. Elsevier, Burlington, pp 1–90

Bai Z, Fan Y (2018) Abnormal strain rate sensitivity driven by a unit dislocation-obstacle interaction in BCC Fe. Phys Rev Lett 120(12):125504

Bai XM, Voter AF, Hoagland RG, Nastasi M, Uberuaga BP (2010) Efficient annealing of radiation damage near grain boundaries via interstitial emission. Science 327(5973):1631–1634

Bakó B, Groma I, Györgyi G, Zimányi G (2006) Dislocation patterning: the role of climb in mesoscale simulations. Comput Mater Sci 38(1):22–28

Barkema GT, Mousseau N (1996) Event-based relaxation of continuous disordered systems. Phys Rev Lett 77(21):4358–4361

Boyle JT, Spence J (2013) Stress analysis for creep. Elsevier, Kent

Brechet Y, Estrin Y (1995) On the influence of precipitation on the portevin-le chatelier effect. Acta Metall Mater 43(3):955–963

Bulatov VV, Hsiung LL, Tang M, Arsenlis A, Bartelt MC, Cai W, Florando JN, Hiratani M, Rhee M, Hommes G, Pierce TG, de la Rubia TD (2006) Dislocation multi-junctions and strain hardening. Nature 440(7088):1174–1178

Campbell JD, Ferguson WG (1970) The temperature and strain-rate dependence of the shear strength of mild steel. Philos Mag 21(169):63–82
Cances E, Legoll F, Marinica MC, Minoukadeh K, Willaime F (2009) Some improvements of the activation-relaxation technique method for finding transition pathways on potential energy surfaces. J Chem Phys 130(11):114711. https://doi.org/10.1063/1.3088532
Cao AJ, Cheng YQ, Ma E (2009) Structural processes that initiate shear localization in metallic glass 57:5146–5155
Cao P, Li M, Heugle RJ, Park HS, Lin X (2012) A self-learning metabasin escape algorithm and the metabasin correlation length of supercooled liquids. Phys Rev E 86:016710
Cao P, Park HS, Lin X (2013) Strain-rate and temperature-driven transition in the shear transformation zone for two-dimensional amorphous solids. Phys Rev E 88(4):042404
Cao P, Lin X, Park HS (2014a) Surface shear-transformation zones in amorphous solids. Phys Rev E 90(1):012311
Cao P, Lin X, Park HS (2014b) Strain-rate and temperature dependence of yield stress of amorphous solids via self-learning metabasin escape algorithm. J Mech Phys Solids 68: 239–250
Cao P, Short MP, Yip S (2017) Understanding the mechanisms of amorphous creep through molecular simulation. Proc Natl Acad Sci 114(52):13631–13636
Cao P, Dahmen KA, Kushima A, Wright WJ, Park HS, Short MP, Yip S (2018) Nanomechanics of slip avalanches in amorphous plasticity. J Mech Phys Solids 114:158–171
Chaari N, Clouet E, Rodney D (2014) First-principles study of secondary slip in zirconium. Phys Rev Lett 112(7):075504
Dezerald L, Rodney D, Clouet E, Ventelon L, Willaime F (2016) Plastic anisotropy and dislocation trajectory in BCC metals. Nat Commun 7:11695
Domain C, Monnet G (2005) Simulation of screw dislocation motion in iron by molecular dynamics simulations. Phys Rev Lett 95(21):215506
Dunlop JW, Bréchet YJM, Legras L, Estrin Y (2007) Dislocation density-based modelling of plastic deformation of zircaloy-4. Mater Sci Eng A 443(1–2):77–86
Dutta A, Bhattacharya M, Gayathri N, Das GC, Barat P (2012) The mechanism of climb in dislocation–nanovoid interaction. Acta Mater 60(9):3789–3798
El-Awady JA, Bulent Biner S, Ghoniem NM (2008) A self-consistent boundary element, parametric dislocation dynamics formulation of plastic flow in finite volumes. J Mech Phys Solids 56(5):2019–2035
Falk ML, Langer JS (1998) Dynamics of viscoplastic deformation in amorphous solids. Phys Rev E 57(6):7192–7205
Falk M, Maloney C (2010) Simulating the mechanical response of amorphous solids using atomistic methods. Eur Phys J B 75(4):405–413
Fan Y (2013) Atomistic simulation of defect structure evolution and mechanical properties at long time scales, Thesis
Fan Y, Osetsky YN, Yip S, Yildiz B (2012) Onset mechanism of strain-rate-induced flow stress upturn. Phys Rev Lett 109(13):135503. https://doi.org/10.1103/PhysRevLett.109.135503
Fan Y, Osetskiy YN, Yip S, Yildiz B (2013) Mapping strain rate dependence of dislocation-defect interactions by atomistic simulations. Proc Natl Acad Sci 110(44):17756–17761
Fan Y, Yip S, Yildiz B (2014) Autonomous basin climbing method with sampling of multiple transition pathways: application to anisotropic diffusion of point defects in HCP Zr. J Phys Condens Matter 26(36):365402
Ferguson WG, Hauser FE, Dorn JE (1967) Dislocation damping in zinc single crystals. Br J Appl Phys 18(4):411
Follansbee PS, Kocks UF (1988) A constitutive description of the deformation of copper based on the use of the mechanical threshold stress as an internal state variable. Acta Metall 36(1):81–93
Follansbee PS, Regazzoni G, Kocks UF (1984) Mechanical properties of materials at high rates of strain (9th ed.). The institute of Physics, Inst Phys Conf Ser, p 71
Gordon PA, Neeraj T, Li Y, Li J (2010) Screw dislocation mobility in BCC metals: the role of the compact core on double-kink nucleation. Model Simul Mater Sci Eng 18(8):085008

Gussev MN, Field KG, Busby JT (2015) Deformation localization and dislocation channel dynamics in neutron-irradiated austenitic stainless steels. J Nucl Mater 460:139–152
Haixuan X, Yuri NO, Roger ES (2012) Self-evolving atomistic kinetic Monte Carlo: fundamentals and applications. J Phys Condens Matter 24(37):375402
Harris MB, Watts LS, Homer ER (2016) Competition between shear band nucleation and propagation across rate-dependent flow transitions in a model metallic glass. Acta Mater 111:273–282
Henkelman G, Jonsson H (1999) A dimer method for finding saddle points on high dimensional potential surfaces using only first derivatives. J Chem Phys 111(15):7010–7022. https://doi.org/10.1063/1.480097
Hoge KG, Mukherjee AK (1977) The temperature and strain rate dependence of the flow stress of tantalum. J Mater Sci 12(8):1666–1672
Huang Y, Shen J, Chiu Y, Chen J, Sun J (2009) Indentation creep of an Fe-based bulk metallic glass. Intermetallics 17(4):190–194
Hull D, Bacon D (2011) Introduction to dislocations (5th ed.). Butterworth-Heinemann, Oxford, ISBN 9780080966724
Iyer M, Radhakrishnan B, Gavini V (2015) Electronic-structure study of an edge dislocation in aluminum and the role of macroscopic deformations on its energetics. J Mech Phys Solids 76:260–275
Jumonji K, Ueta S, Miyahara A, Kato M, Sato A (1996) Rapid work hardening caused by cube cross slip in Ni3Al single crystals. Philos Mag A 73(2):345–364
Kabir M, Lau TT, Rodney D, Yip S, Van Vliet KJ (2010) Predicting dislocation climb and creep from explicit atomistic details. Phys Rev Lett 105(9):095501
Kioussis NG, Ghoniem NM (2010) Modeling of dislocation interaction with solutes, nano-precipitates and interfaces: a multiscale challenge. J Comput Theor Nanosci 7(8):1317–1346
Klueh R (2005) Elevated temperature ferritic and martensitic steels and their application to future nuclear reactors. Int Mater Rev 50(5):287–310
Kocks UF, Argon AS, Ashby MF (1975) Thermodynamics and Kinetics of Slip (9th ed.). Pergamon Press, New York. Prog Mater Sci, 19(9):p. 110
Krisponeit J-O, Pitikaris S, Avila KE, Küchemann S, Krüger A, Samwer K (2014) Crossover from random three-dimensional avalanches to correlated nano shear bands in metallic glasses. Nat Commun 5:3616
Kumar A, Hauser FE, Dorn JE (1968) Viscous drag on dislocations in aluminum at high strain rates. Acta Metall 16(9):1189–1197
Kushima A, Lin X, Li J, Eapen J, Mauro JC, Qian X, Diep P, Yip S (2009a) Computing the viscosity of supercooled liquids. J Chem Phys 130(22):224504
Kushima A, Lin X, Li J, Qian X, Eapen J, Mauro JC, Diep P, Yip S (2009b) Computing the viscosity of supercooled liquids. II. Silica and strong-fragile crossover behavior. J Chem Phys 131(16):164505–164509
Laio A, Parrinello M (2002) Escaping free-energy minima. Proc Natl Acad Sci 99(20):12562–12566
Lebensohn RA, Tomé CN, CastaÑeda PP (2007) Self-consistent modelling of the mechanical behaviour of viscoplastic polycrystals incorporating intragranular field fluctuations. Philos Mag 87(28):4287–4322
Lebyodkin MA, Brechet Y, Estrin Y, Kubin LP (1995) Statistics of the catastrophic slip events in the portevin-le chatelier effect. Phys Rev Lett 74(23):4758–4761
Lu J, Ravichandran G, Johnson WL (2003) Deformation behavior of the Zr 41.2 Ti 13.8 Cu 12.5 Ni 10 Be 22.5 bulk metallic glass over a wide range of strain-rates and temperatures. Acta Mater 51(12):3429–3443
Maaß R, Klaumünzer D, Löffler J (2011) Propagation dynamics of individual shear bands during inhomogeneous flow in a Zr-based bulk metallic glass. Acta Mater 59(8):3205–3213
Matsukawa Y, Zinkle SJ (2004) Dynamic observation of the collapse process of a stacking fault tetrahedron by moving dislocations. J Nucl Mater 329–333, Part B(0):919–923

Mendelev MI, Han S, Srolovitz DJ, Ackland GJ, Sun DY, Asta M (2003) Development of new interatomic potentials appropriate for crystalline and liquid iron. Philos Mag 83(35):3977–3994
Needleman A, Van der Giessen E (2005) Elasticity: finite element modeling A2 – Buschow, K.H. Jürgen. Elsevier, Oxford, pp 1–6
Nieh T, Wadsworth J (2006) Homogeneous deformation of bulk metallic glasses. Scr Mater 54(3):387–392
Norfleet DM, Dimiduk DM, Polasik SJ, Uchic MD, Mills MJ (2008) Dislocation structures and their relationship to strength in deformed nickel microcrystals. Acta Mater 56(13):2988–3001
Onimus F, Béchade J-L (2009) A polycrystalline modeling of the mechanical behavior of neutron irradiated zirconium alloys. J Nucl Mater 384(2):163–174
Onimus F, Monnet I, Béchade JL, Prioul C, Pilvin P (2004) A statistical TEM investigation of dislocation channeling mechanism in neutron irradiated zirconium alloys. J Nucl Mater 328(2–3):165–179
Osetsky YN, Matsukawa Y, Stoller RE, Zinkle SJ (2006a) On the features of dislocation–obstacle interaction in thin films: large-scale atomistic simulation. Philos Mag Lett 86(8):511–519
Osetsky YN, Rodney D, Bacon DJ (2006b) Atomic-scale study of dislocation–stacking fault tetrahedron interactions. Part I: mechanisms. Philos Mag 86(16):2295–2313
Preston DL, Tonks DL, Wallace DC (2003) Model of plastic deformation for extreme loading conditions. J Appl Phys 93(1):211–220
Proville L, Rodney D, Marinica M-C (2012) Quantum effect on thermally activated glide of dislocations. Nat Mater 11(10):845–849
Regazzoni G, Kocks UF, Follansbee PS (1987) Dislocation kinetics at high strain rates. Acta Metall 35(12):2865–2875
Remington BA, Allen P, Bringa EM, Hawreliak J, Ho D, Lorenz KT, Lorenzana H, McNaney JM, Meyers MA, Pollaine SW, Rosolankova K, Sadik B, Schneider MS, Swift D, Wark J, Yaakobi B (2006) Material dynamics under extreme conditions of pressure and strain rate. Mater Sci Technol 22(4):474–488
Rodney D, Proville L (2009) Stress-dependent peierls potential: influence on kink-pair activation. Phys Rev B 79(9):094108
Schuh C, Nieh T, Kawamura Y (2002) Rate dependence of serrated flow during nanoindentation of a bulk metallic glass. J Mater Res 17(7):1651–1654
Schuh CA, Hufnagel TC, Ramamurty U (2007) Mechanical behavior of amorphous alloys. Acta Mater 55(12):4067–4109
Schwarz KW (1999) Simulation of dislocations on the mesoscopic scale. I. Methods and examples. J Appl Phys 85(1):108–119
Sentjabrskaja T, Chaudhuri P, Hermes M, Poon W, Horbach J, Egelhaaf S, Laurati M (2015) Creep and flow of glasses: strain response linked to the spatial distribution of dynamical heterogeneities. Sci Rep 5:11884
Shan Z, Li J, Cheng Y, Minor A, Asif SS, Warren O, Ma E (2008) Plastic flow and failure resistance of metallic glass: insight from in situ compression of nanopillars. Phys Rev B 77(15):155419
Shin CS, Fivel MC, Verdier M, Robertson C (2005) Dislocation dynamics simulations of fatigue of precipitation-hardened materials. Mater Sci Eng A 400–401:166–169
Siebenbürger M, Ballauff M, Voigtmann T (2012) Creep in colloidal glasses. Phys Rev Lett 108(25):255701
Sorensen MR, Voter AF (2000) Temperature-accelerated dynamics for simulation of infrequent events. J Chem Phys 112(21):9599–9606
Spaepen F (1977) A microscopic mechanism for steady state inhomogeneous flow in metallic glasses. Acta Metall 25(4):407–415
Steinberg DJ, Lund CM (1989) A constitutive model for strain rates from 10[sup - 4] to 10[sup 6] s[sup - 1]. J Appl Phys 65(4):1528–1533
Suo Z (2000) Evolving material structures of small feature sizes. Int J Solids Struct 37(1):367–378
Tao W, Cao P, Park HS (2018a) Atomistic simulation of the rate-dependent ductile-to-brittle failure transition in bicrystalline metal nanowires. Nano lett 18(2):1296–1304

Tao W, Cao P, Park HS (2018b) Superplastic creep of metal nanowires from rate-dependent plasticity transition. ACS nano 12(5):4984–4992

Terentyev D, Grammatikopoulos P, Bacon DJ, Osetsky YN (2008) Simulation of the interaction between an edge dislocation and a< 1 0 0> interstitial dislocation loop in α-iron, Acta Materialia 56(18):5034–5046

Terentyev D, Osetsky YN, Bacon DJ (2010a) Competing processes in reactions between an edge dislocation and dislocation loops in a body-centred cubic metal. Scr Mater 62(9):697–700

Terentyev D, Bonny G, Domain C, Pasianot RC (2010b) Interaction of a 1/2< 111> screw dislocation with Cr precipitates in BCC Fe studied by molecular dynamics. Phys Rev B 81(21):214106

Turner PA, Tomé CN, Christodoulou N, Woo CH (1999) A self-consistent model for polycrystals undergoing simultaneous irradiation and thermal creep. Philos Mag A 79(10):2505–2524

Van der Giessen E, Deshpande VS, Cleveringa HHM, Needleman A (2001) Discrete dislocation plasticity and crack tip fields in single crystals. J Mech Phys Solids 49(9):2133–2153

Voter AF (1997) A method for accelerating the molecular dynamics simulation of infrequent events. J Chem Phys 106(11):4665–4677

Wang H, Xu DS, Rodney D, Veyssire P, Yang R (2013) Atomistic investigation of the annihilation of non-screw dislocation dipoles in al, cu, ni and γ-tial. Model Simul Mater Sci Eng 21(2):025002

Wei Y, Zhigang S (1996) Global view of microstructural evolution: energetics, kinetics and dynamical systems. Acta Mech Sinica 12(2):144–157

Wright WJ, Byer RR, Gu X (2013) High–speed imaging of a bulk metallic glass during uniaxial compression. Appl Phys Lett 102(24):241920

Wright WJ, Liu Y, Gu X, Van Ness KD, Robare SL, Liu X, Antonaglia J, LeBlanc M, Uhl JT, Hufnagel TC et al (2016) Experimental evidence for both progressive and simultaneous shear during quasistatic compression of a bulk metallic glass. J Appl Phys 119(8):084908

Yamakov V, Wolf D, Phillpot SR, Mukherjee AK, Gleiter H (2002) Dislocation processes in the deformation of nanocrystalline aluminium by molecular-dynamics simulation. Nat Mater 1(1):45–49

Yan X, Cao P, Tao W, Sharma P, Park HS (2016) Atomistic modeling at experimental strain rates and timescales. J Phys D Appl Phys 49(49):493002

Yip S (2003) Synergistic science. Nat Mater 2(1):3–5

Yip S (2016) Understanding the viscosity of supercooled liquids and the glass transition through molecular simulations. Mol Simul 42(16):1330–1342

Yip S, Short MP (2013) Multiscale materials modelling at the mesoscale. Nat Mater 12(9):774

Zbib HM, de la Rubia TD (2002) A multiscale model of plasticity. Int J Plast 18(9):1133–1163

Zerilli FJ, Armstrong RW (1987) Dislocation-mechanics-based constitutive relations for material dynamics calculations. J Appl Phys 61(5):1816–1825

Zhong Y, Zhu T (2008) Simulating nanoindentation and predicting dislocation nucleation using interatomic potential finite element method. Comput Methods Appl Mech Eng 197(41–42): 3174–3181

Zhu T, Li J, Samanta A, Leach A, Gall K (2008) Temperature and strain-rate dependence of surface dislocation nucleation. Phys Rev Lett 100(2):025502